

Supplementary Information

Minimizing polymorphic risk through cooperative computational and experimental exploration

Christopher R. Taylor, ‡^a Matthew T. Mulvee, ‡^b Domonkos S. Perenyi,^b Michael R. Probert,^{*c} Graeme M. Day^{*a} and Jonathan W. Steed^{*b}

Experimental

Templated sublimations

The powder of the sample being sublimated was placed on a glass slide and then a Linkam LTS420 heating stage and the templating crystal was affixed to a borosilicate glass coverslip with a small amount of Vaseline and then separated from the glass slide with a small rubber o-ring. The powders were then heated to a temperature to achieve sublimation, 131 °C for iproniazid (IPN) and 141 °C for isoniazid (ISN) at either 5 or 10 °C/min for 6 hours for to ensure all the sample sublimates and then the sample was left overnight to allow for crystal growth.

Synthesis of gelators

Gelator 1: Prepared as reported previously.¹ Isoniazid (0.5 g, 3.65 mmol) and 4,4-methylenebis(2,6-diethylphenyl isocyanate) (0.66 g, 1.82 mmol) were dissolved in the mixture of chloroform and ethanol (30 mL : 3 mL) and triethylamine (1 mL, 7.17 mmol) was added slowly. The solution was heated and refluxed for 24 h. The resulting precipitate was washed with CHCl₃ (3 x 20 ml) and dried using a drying piston. The product appeared as a slightly beige, white powder (0.92 g, 1.44 mmol, 79%). ¹H NMR (400 MHz, DMSO-*d*₆) δ 10.57 (s, 2H, NH), 8.77 – 8.71 (m, 4H, Ar-H), 8.21 (s, 2H, NH), 8.00 (s, 2H, NH), 7.83 (d, J = 5.1 Hz, 4H, Ar-H), 6.94 (s, 4H, Ar-H), 3.84 (d, 2H, C-H₂), 2.55-2.50 (m, 8H, CH₂CH₃), 1.08 (t, 12H, CH₂CH₃); ¹³C{¹H} NMR (101 MHz, DMSO-*d*₆) δ 165.46 (C=O), 150.66 (ArC), 142.69 (ArC), 140.29 (ArC), 132.31 (ArC), 126.66 (ArC), 122.01 (ArC), 41.18 (Ar-CH₂-Ar), 24.80 (CH₂CH₃), 15.27 (CH₂CH₃). ESI-MS: M+H⁺ *m/z* 638.6

Gelator 2: L-Tyrosine methyl ester (0.5 g, 2.56 mmol) and 4,4-methylenebis(2,6-diethylphenyl isocyanate) (0.46 g, 1.28 mmol) were dissolved in THF (150 mL). The solution was heated and refluxed for 24 hours. The resulting precipitate was washed with THF (3 x 15 ml) and DCM (3 x 20 ml) and dried using the drying piston. The product appeared as a pale white powder (0.72 g, 1.04 mmol, 81%). ¹H NMR (400 MHz, DMSO-*d*₆) δ 9.25 (s, 2H, NH), 7.53 (s, 2H, NH), 6.96 (m, 4H, Ar-H), 6.91 (s, 4H, Ar-H), 6.68 (s, 4H, Ar-H), 6.36 (s, 2H, OH) 4.39 (q, 2H, N-CH), 3.81 (s, 2H, Ar-CH₂-Ar), 3.61 (s, 6H, O-CH₃), 2.88 (d, 6H, Ar-CH₂-CH), 2.44-2.42 (q, 8H, CH₃-CH₂-), 1.05 (t, 12H, CH₃-CH₂) ¹³C{¹H} NMR (101 MHz, DMSO-*d*₆) δ 173.34 (OC=O), 156.51 (NC=O), 130.59 (ArC), 127.38 (ArC), 126.65 (ArC), 115.50 (ArC), 54.66 (O-CH₃), 46.13 (Ar-CH₂-Ar), 24.86 (CH₂-CH₃), 15.15 (CH₂-CH₃). ESI-MS: M+H⁺ *m/z* 697.4 M+IsoProp+H⁺ *m/z* 7537.

Gelator 3: Prepared as reported previously.² 5-Aminosalicylic acid (0.5 g, 3.27 mmol) was dissolved in chloroform and ethanol (15 mL:1.5 mL) and 4,4'-methylenebis(2,6-diethylaniline) (0.59 g, 1.63 mmol) was added. Triethylamine (0.78 mL, 5.59 mmol) was added slowly to give a solution that was heated under reflux for 12 h. The resulting suspension was then filtered and washed with chloroform (100 mL) to give an off-white solid. This compound was triturated in aqueous HCl (1 M, 250 mL) for 30 minutes, filtered and washed with chloroform (3 x 25 ml) to give a slightly pink solid which was isolated by filtration and air dried (0.57 g, 0.85 mmol, 52%). ¹H NMR (400 MHz, DMSO-*d*₆) δ 10.06 (bs, 2H, CO₂H), 8.64 (s, 2H, OH), 7.73 (s, 2H, NH), 7.66 (s, 2H, NH), 7.35 (d, 2H, Ar-H), 6.98 (s, 6H, Ar-H), 6.64 (d, J = 8.7 Hz, 2H, Ar-H), 3.85 (s, 2H Ar-CH₂-Ar), 2.53 (q, 8H, CH₂CH₃), 1.11 (t, 12H, CH₂CH₃); ¹³C{¹H} NMR (101 MHz, DMSO-*d*₆) δ 172.21 (CO₂H), 162.90 (C=O), 153.88 (ArC), 148.09 (ArC), 131.41 (ArC), 128.17 (ArC), 123.10 (ArC), 121.72 (ArC), 109.22 (ArC), 105.81 (ArC), 55.19 (Ar-CH₂-Ar), 30.07 (CH₂-CH₃), 15.17 (CH₂-CH₃); ESI-MS: M-H⁻ *m/z* 667.8 M+H⁺ 669.5

Gelator 4: Prepared as reported previously.³ 1,3-Bis(1-isocyanato-1-methylethyl) benzene (2.00 g, 8.2 mmol) was dissolved in dry CHCl₃ (40 mL) using heating to reflux under N₂ atmosphere. (3-aminopropyl) triethoxysilane (3.65 g, 16.4 mmol) was dissolved in dry CHCl₃ (40 mL) and was added dropwise to the reaction mixture. Then the reaction mixture was then left stirring under reflux for 24 h. After 24 h the solvent has completely evaporated, and the

resulting white powder was washed with CHCl_3 (3 x 20 mL) and THF (3 x 40 mL). The product appeared as a bright white powder. (4.62 g, 6.72 mmol, 82 %) ^1H NMR (400 MHz, $\text{DMSO}-d_6$) δ 7.32-7.27 (m, 1H, Ar-H), 7.24-7.14 (m, 3H, Ar-H), 6.13-6.11 (d, 2H, NH), 6.04-6.01 (t, 2H, NH), 3.74 (q, 12H, O-CH₂-), 2.88-90 (dd, 4H, NH-CH₂-) 1.41-1.35 (m, 4H, -CH₂-), 1.15z (t, 18H, CH₃). $^{13}\text{C}\{^1\text{H}\}$ NMR (101 MHz, $\text{DMSO}-d_6$) δ 157.59 (C=O), 148.96 (ArC), 127.65 (ArC), 122.75 (ArC), 121.77 (ArC), 58.15 (O-CH₂-CH₃), 54.68 (Ar-C-NH), 42.09 (Ar-CH₂-NH), 30.62 (C-CH₃), 24.12 (CH₂-CH₂-CH₂), 18.68 (CH₂-CH₃). 7.73 (CH₂-CH₂-Si) ESI-MS: $\text{M}+\text{Na}^+$ m/z 709.4

Materials

All reagents, active pharmaceutical ingredients and solvents were purchased from standard commercial sources and were used without further purification.

Instrumentation

Powder X-ray diffraction measurements (pXRD) were performed by mounting powders onto silicon single crystal wafer slides and were using either a Bruker D8 powder X-ray diffractometer in Bragg-Brentano geometry. Samples were mounted on a silicon single crystal wafer and analysed using $\text{Cu}-\text{K}\alpha$ radiation at a wavelength of 1.5406 Å. X-rays were produced using an operating voltage of 40 kV and a current of 40 mA. Samples were scanned over an angle range of 5-50° 2 θ at a scan rate of 0.02° step⁻¹. X-ray single-crystal data for Forms I and II were collected at 120.0(2) K using graphite monochromated Mo $\text{K}\alpha$ radiation ($\lambda = 0.71073\text{Å}$) on a Bruker D8 Venture (Photon100 CMOS detector, μS -microsource, focusing mirrors) diffractometer equipped with a Cryostream 700+ (Oxford Cryosystems) open-flow nitrogen cryostat. Single crystals were coated in perfluoro polyether oil, mounted on a MiTeGen sample holder and placed directly into the precooled cryostream. Structures were solved by direct methods and refined by full-matrix least squares on F2 against all data using Olex2⁴ and SHELXT⁵ software. All non-hydrogen atoms were refined anisotropically, hydrogen atoms in structures were placed in the calculated positions and refined in riding mode. NMR spectra were obtained using a Bruker Avance 400 spectrometer at room temperature. Mass spectra were obtained using a Waters Ltd. TQD spectrometer. Mass spectrometry samples were prepared as 1 mg mL⁻¹ solutions of the solute in acetonitrile or methanol. Elemental analysis was performed on 5 mg of sample using an Exeter CE-440 Elemental analyser by Dr. Emily Unsworth.

High-pressure experiments

High-pressure experiments were conducted by compressing crystals that were grown at ambient pressure in a Merrill-Bassett diamond anvil cell (DAC)⁶ using Fluorinert™ FC-70 as an inert pressure transmitting fluid. A stainless steel gasket, 250 μm thick, was pre-indented to ca. 150 μm and drilled with a 300 μm precision hole to create the sample chamber between the two diamond anvils, culet size of 800 μm . A ruby sphere was included in the sample chamber for pressure determination. The pressure inside the cell was measured after equilibration using a ruby sphere included in the sample chamber by the R₁ ruby fluorescence method.⁷ The diamond anvil cell was directly attached to a goniometer head and mounted on the diffractometer. Data were collected using the XIPHOS II diffractometer at Newcastle University, a four-circle Huber Eulerian goniometer with offset chi cradle fitted with a Bruker APEXII CCD area detector and an Ag- $\text{K}\alpha$ μS generator. Data collections of crystals in DACs is poor at locating H-atom positions due to shading by the gasket and DAC, which reduces the completeness of the dataset.⁸⁻¹⁰

Hirschfeld surface analysis

Hirshfeld surfaces and fingerprint plots are a useful way to visualize and compare the intermolecular interactions and packing of different crystal structures. The Hirshfeld surface is the boundary where the electron distribution of the promolecule (sum of spherical atom electron densities for a molecule) dominates over the procrystal (the same sum over the whole crystal).¹¹⁻¹³ These surfaces map the distances of atoms external (d_e) and internal (d_i) to the surface, but typically d_{norm} is used as this contact distance is normalized for the different vdW radii of different elements.¹² As it is non-trivial to analyse these 3D surfaces they are often summarized as 2D fingerprint plots.¹¹ Together these methods allow for easy comparison of the intermolecular interactions and packing of different forms without biasing particular interactions *i.e.* H-bonding. All plots appear to be pseudo-symmetric, which is due to the close packing of the Hirshfeld surfaces so that where the surfaces touch, both of the points (d_i , d_e) and (d_e , d_i) will appear on the 2D-graph.^{11,14} However, as these surfaces are smooth, small voids are left where no single molecule dominates and thus d_e is often larger than d_i .¹¹ All surfaces and fingerprint plots were created using the Crystal Explorer Software.¹⁵ CrystalExplorer uses normalized X-H bond lengths using data from neutron diffraction experiments.¹³

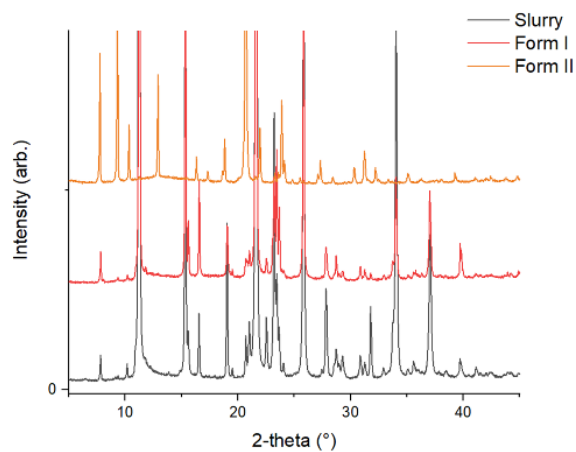


Figure S1 pXRD patterns for IPN Form I (red), Form II (orange) and the resulting powder from the slurry experiment (black) demonstrating that only Form I remains. Note the absence of the peaks at 9.3°, 12.9°, 30.3°

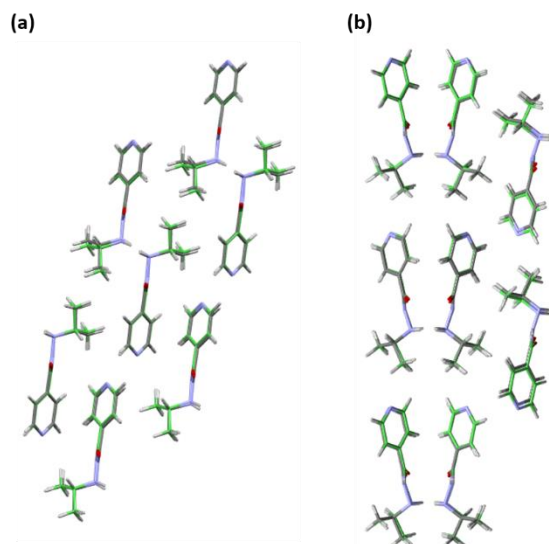


Figure S2 Overlays of IPN crystal structures from experimental data and predicted CSP structures using the CSD-Material Crystal Structure Similarity feature of Mercury.¹⁹ In both cases a 15 molecules cluster was used with a 20% distance tolerance and 20° angle tolerance. (a) Form I vs. CSP Structure 2 and (b) Form II vs. CSP Structure 5. For both structures 15 out of 15 structures matched indicating they are the same crystal structures.

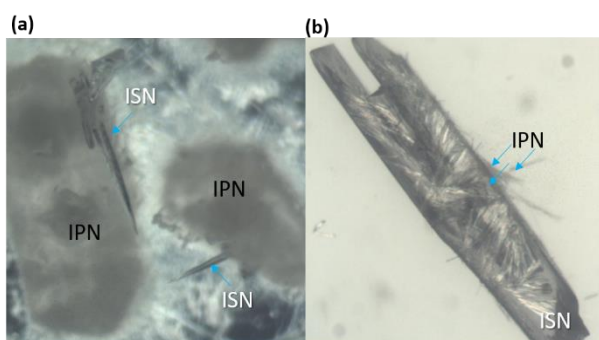


Figure S3 Photos of template sublimations (a) ISN crystals growing from IPN crystals and (b) IPN crystals grown from an ISN crystal.

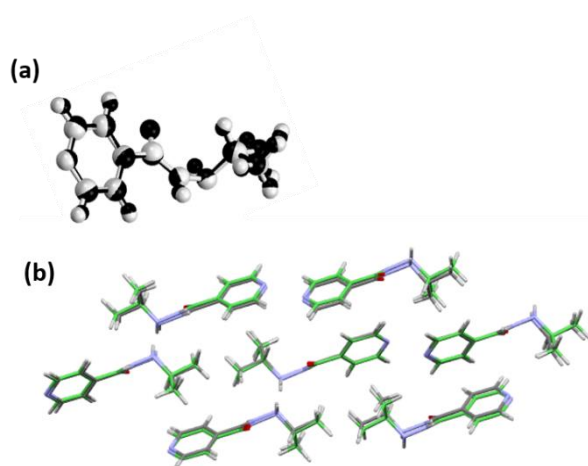


Figure S4 Overlay of CSP predicted structure and experimental IPN Form III (a) molecule overlay and (b) packing overlay, demonstrating that the same conformation and crystal packing is observed for Form III.

Table S1 Crystallographic Data for Form II recorded at different pressures and temperatures.

Crystal Form	Form II	Form II	Form II
Formula	C ₉ H ₁₃ N ₃ O	C ₉ H ₁₃ N ₃ O	C ₉ H ₁₃ N ₃ O
Molecular weight /g mol ⁻¹	179.219	179.219	179.219
Crystal System	Orthorhombic	Orthorhombic	Monoclinic
Space Group	Pbca	Pbca	Pbca
T/K	120	291.15	291.15
Pressure/ GPa	ambient	ca. 0	0.3
a/Å	4.9965(7)	5.14	5.02
b/Å	22.845(3)	23.61	22.94
c/Å	16.828(3)	17.47	17.14
α/°	90.000	90.000	90.000
β/°	90.000	90.000	90.000
γ/°	90.000	90.000	90.000
V/Å ³	1921.7(5)	2120.1	

Table S2 Crystallographic Data for Form III at high pressure and then data from the same crystal after decompression to ambient pressure

Crystal Form	Form III	Form III
Formula	C ₉ H ₁₃ N ₃ O	C ₉ H ₁₃ N ₃ O
Molecular weight /g mol ⁻¹	179.219	179.219
Crystal System	Monoclinic	Monoclinic
Space Group	P2 ₁ /c	P2 ₁ /c
T/K	291	291
Pressure/ GPa	2.21	ambient
a/Å	11.240(5)	11.957(2)
b/Å	5.043(3)	5.1538(9)
c/Å	15.171(14)	15.883(3)
α/°	90	90
β/°	109.14(7)	105.547(8)
γ/°	90	90
V/Å ³	812.4(10)	943.0(3)
Z	2	2
Z'	1	1
ρ _{calc} /g cm ⁻³	1.465	1.262
independent reflections	287 [R _{int} = 0.0851]	261 [R _{int} = 0.0105]
goodness-of-fit	1.082	1.175
final R indexes [I ≥ 2σ(I)]	R ₁ = 0.0987 wR ₂ = 0.2524	R ₁ = 0.0819 wR ₂ = 0.2316
final R indexes [all data]	R ₁ = 0.1434 wR ₂ = 0.2863	R ₁ = 0.0841 wR ₂ = 0.2345
CCDC code	2011027	2011028

Extended crystal packing and Hirschfeld surface analysis

Though the fingerprint plots of the three IPN polymorphs are similar, indicative of comparable packing subtle differences explain the more optimal packing of high-pressure Form III versus to the ambient Forms I and II. The sharp peaks observed at the bottom left-hand corner of the fingerprint plots in all are the H-bonding interactions, with the N···H interaction being the bottom of the two, and the other being O···H interactions the shortest contact for all IPN forms. Thus, two spikes are observed for all IPN forms and only one for ISN. As discussed in the main text, the H-bonding is very similar for all IPN forms but is markedly different from that of ISN.

Differences in the 'wings' of the plots in the bottom right and top left are indicative of different stacking of the pyridyl groups (Fig S8). Displaced parallel π-π stacking is present for Form I, whereas offset edge to face stacking is

observed for Form II. Due to the close packing, both stacking geometries are observed for Form III. This corresponds to a notable shift of the d_i and d_e being significantly shorter than the other forms in the fingerprint plots (Fig. S6).

The compression Form I to produce Form III shortens the a-axis and closer packing of the sheets, which results in the filling of the void observed in Form I down the b-axis (Fig S9c); the denser packing is also illustrated in the fingerprint plots. Significant asymmetry is observed in the top right of the fingerprint plots for Form I and II which is indicative of voids and non-optimal packing. The transformation to Form III under hydrostatic pressure largely removes this region with the plot becoming noticeably more symmetrical about the x/y diagonal and in general the data points move to the bottom left (Fig. S6). Which is indicative of more optimal, denser packing.

The Hirshfeld surfaces demonstrate the close packing in Form III (Fig S5). For instance, for Forms I and II, much of the surface is blue indicating that the contact distances are greater than the van der Waals' radii, with red regions indicating short contacts (*e.g.* H-bonding). However, for Form III many such short-contact regions are present around the surface, most notably at the pyridyl group and the hydrogen atoms of the isopropyl group, indicating very close contact between the IPN molecules. These correspond to a sharp feature in the bottom left of the x/y diagonal. For the isopropyl group, these are due to close C-H...H-C contacts between IPN molecules in the H-bonding chains. These contacts are significantly shortened on conversion from Form I (2.503 Å) to Form III (2.225 Å) and are approaching the distance that these interactions would become repulsive (*cf. ab initio* calculations predict the collinear C-H...H-C methane interactions becoming repulsive at distances between 2.1-2.2 Å).^{16,17} Furthermore, the separation between the displaced parallel pyridyl groups shortens from 3.394 Å to 3.275 Å for Forms I and III (measuring the same (pyridyl)C...C(pyridyl) separation distance), respectively. Calculations by several groups using various basis sets at MP2 level have determined that the most stable interaction energies are for separations of *ca.* 3.75 Å measuring the distance from the centre of two pyridyl rings, with these interactions becoming repulsive at separations less than *ca.* 3.3 Å.¹⁸⁻²⁰

This denser packing is visualized with the void function of Mercury²¹ and provides a quantitative comparison between the different forms (Fig. S7). With a probe radius of 0.6 Å and a grid spacing of 0.2 Å, the voids account for 10.2% of the unit cell for Form I and 13.3% for Form II compared to just 0.9% for Form III. These differences are likely to be due to different packing but also because these structures were determined at different temperatures and pressures. Importantly, the CSP structures, generated at 0 K and ambient pressure, also demonstrate differences. For Form I the void space 3.8% compared to 1.6% for Form III. The probes used here are in line with previous studies comparing voids present in ambient and high-pressure forms.^{22,23} Note this void percentage is not a measure of porosity, as a probe at least the size of a hydrogen atom (1.17Å) would be necessary to meaningfully explore accessible void space.²⁴

Table S3 Contact Lengths

Contact	ISN (Å)	IPN Form I (Å)	IPN Form II (Å)	IPN Form III (Å)
C=O...H-N	N/A	2.079	2.007	2.057
N...HN	1.974	2.518	2.647	2.457

Note that these measurements are measurements from models of data collected at different temperatures and pressures. (Forms I and II were recorded at ambient pressure at 120 K whereas Form III was recorded at 291.15 K and a pressure of 2.21 GPa.)

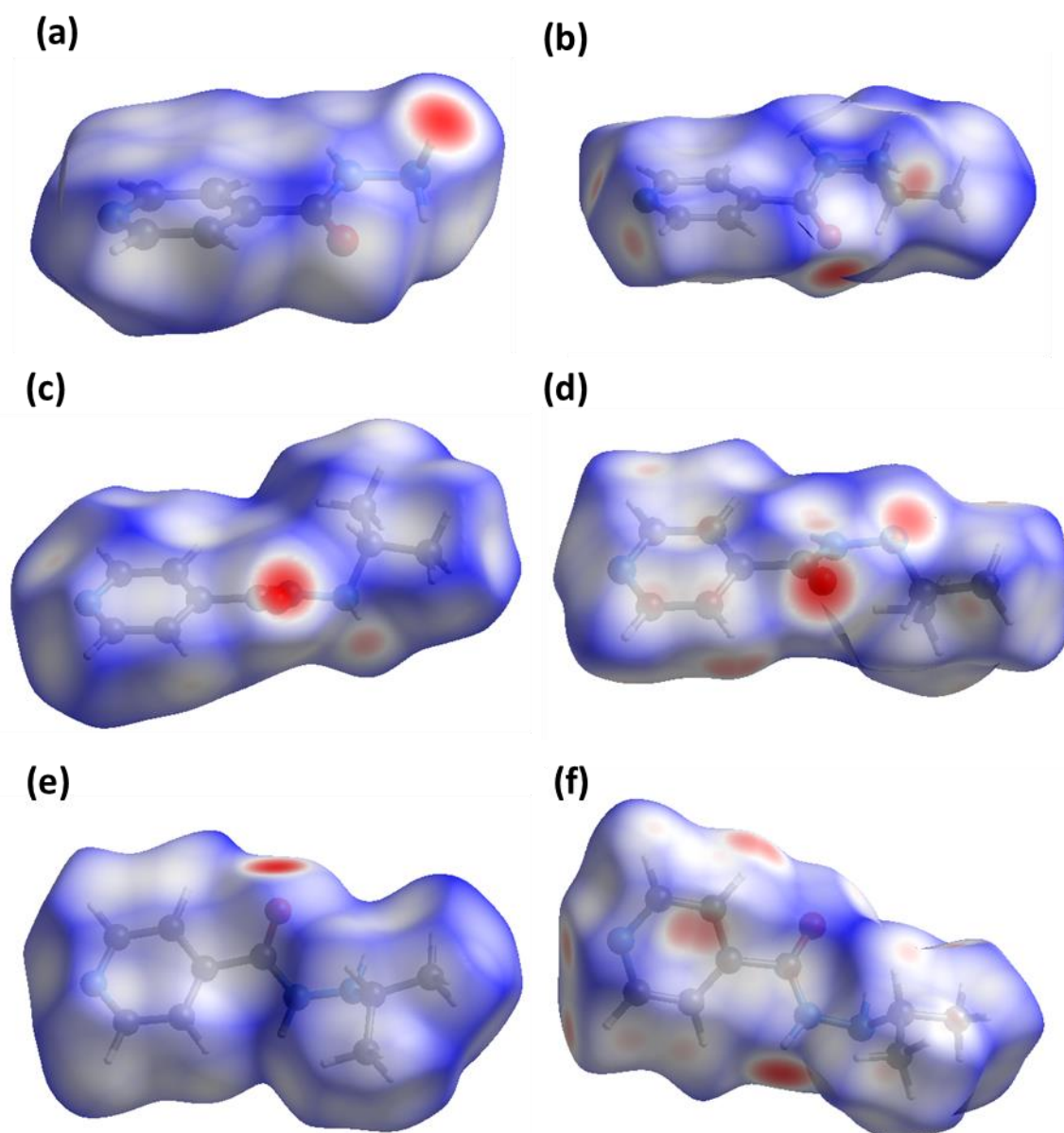


Figure S5 Hirshfeld surfaces mapped with d_{norm} of (a) ISN and IPN (b) Form I, (c) Form II and (d) Form III. As well as alternative orientations of (e) Form I and (f) Form III. White areas of the surface indicate distances equal to vdW radii and blue and red represent contacts longer or shorter than vdW, respectively.

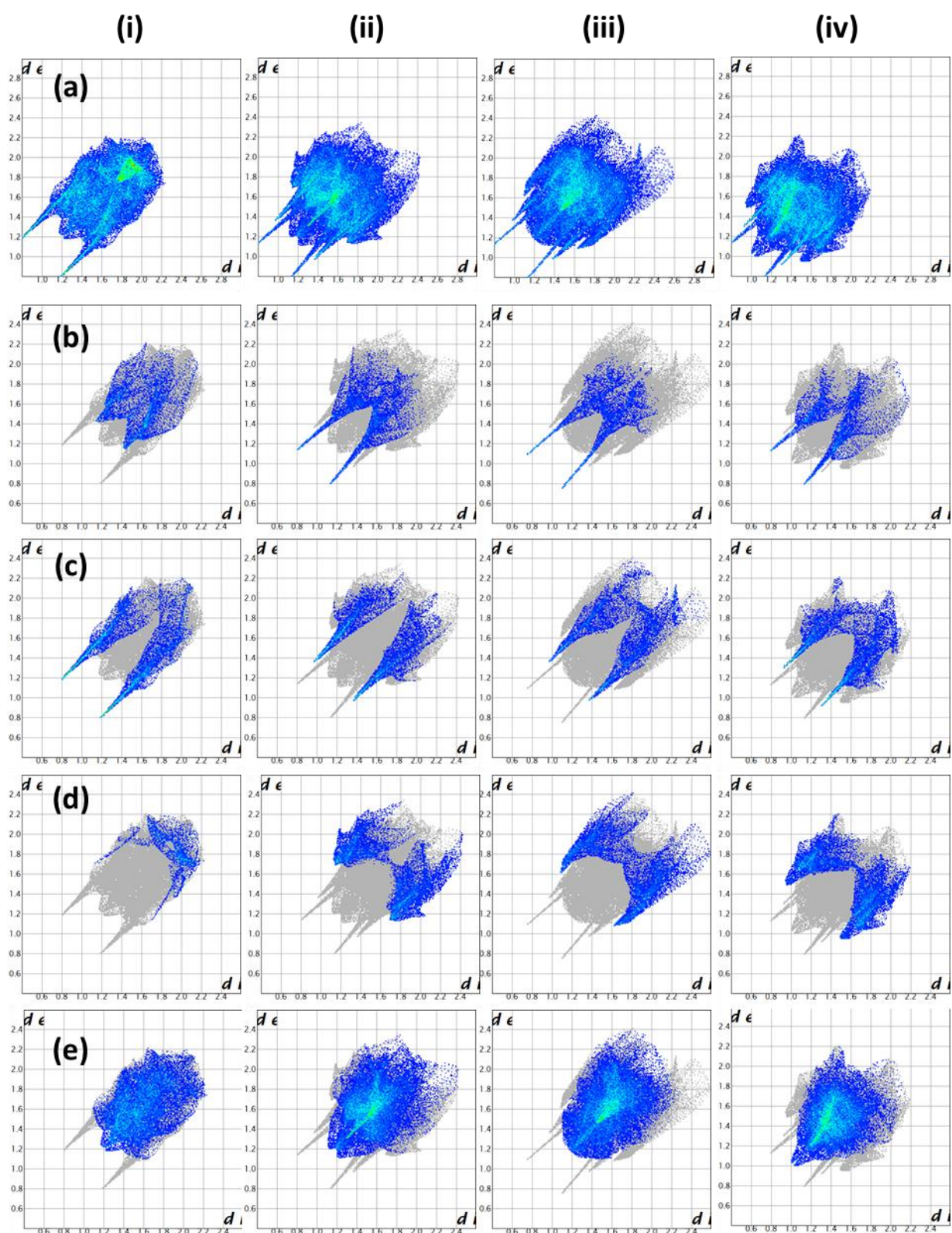


Figure S6 Hirschfeld 2D fingerprint plots of (i) ISN, (ii) IPN-I, (iii) IPN-II and (iv) IPN-III (a) Whole surface, (b) O...H interactions, (c) N...H interactions, (d) C...H interactions and (e) H...H interactions.

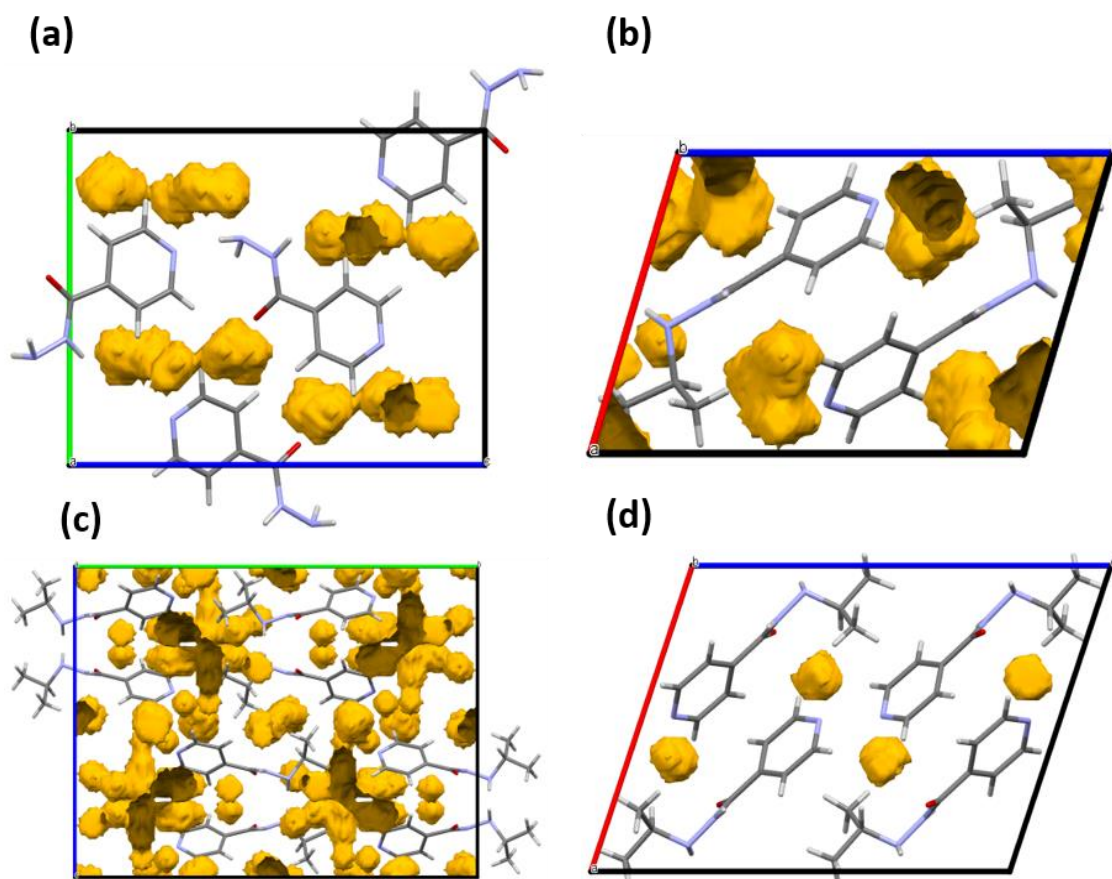


Figure S7 Void space visualised in Mercury for (a) ISN and IPN (b) Form I, (c) Form II (d) Form III. Using a probe radius of 0.6 Å and a grid spacing: 0.2 Å

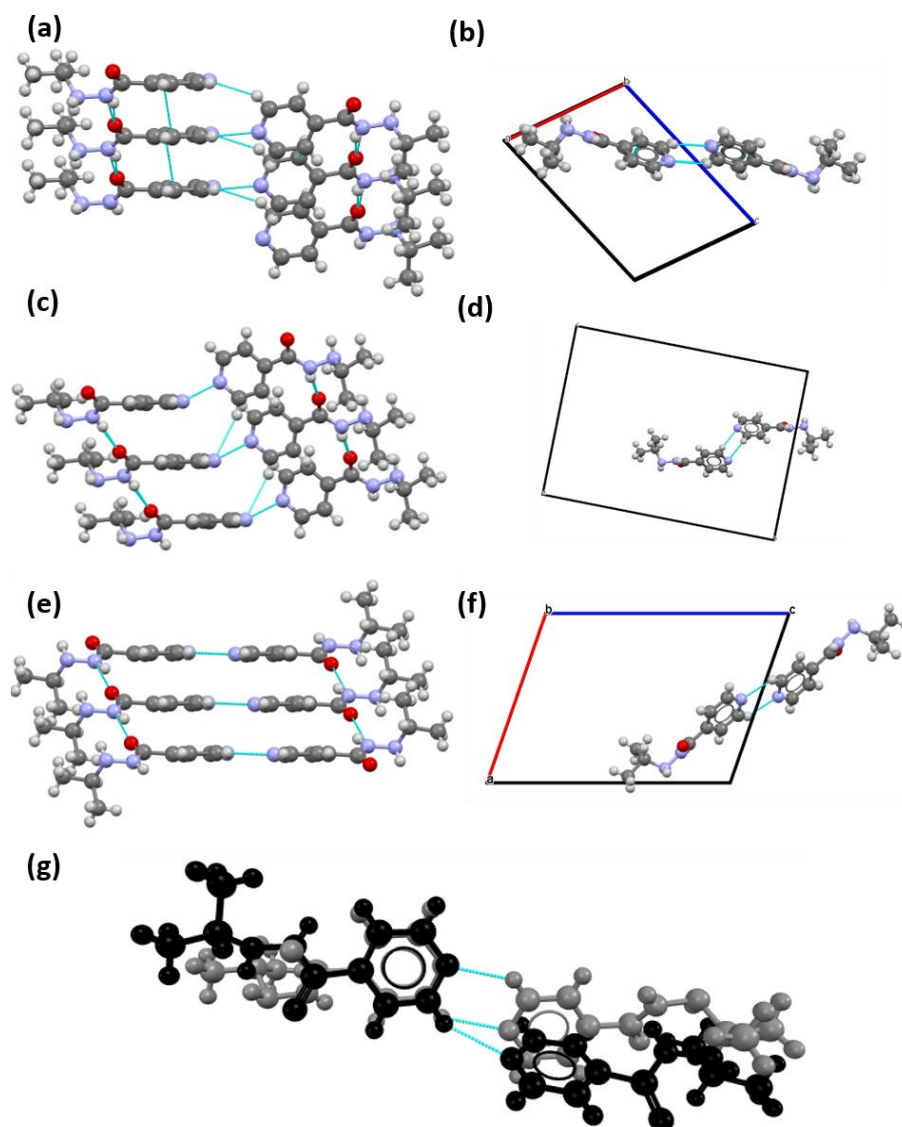


Figure S8 Interactions between pyridyl groups of IPN for (a)-(b) Form I, (c)-(d) Form II and (e)-(f) Form III. Blue lines indicate interactions that were applied using Mercury software. (g) Comparison of the pyridyl contacts for Form I (black) and Form III (grey), demonstrating the closer contacts for the latter.

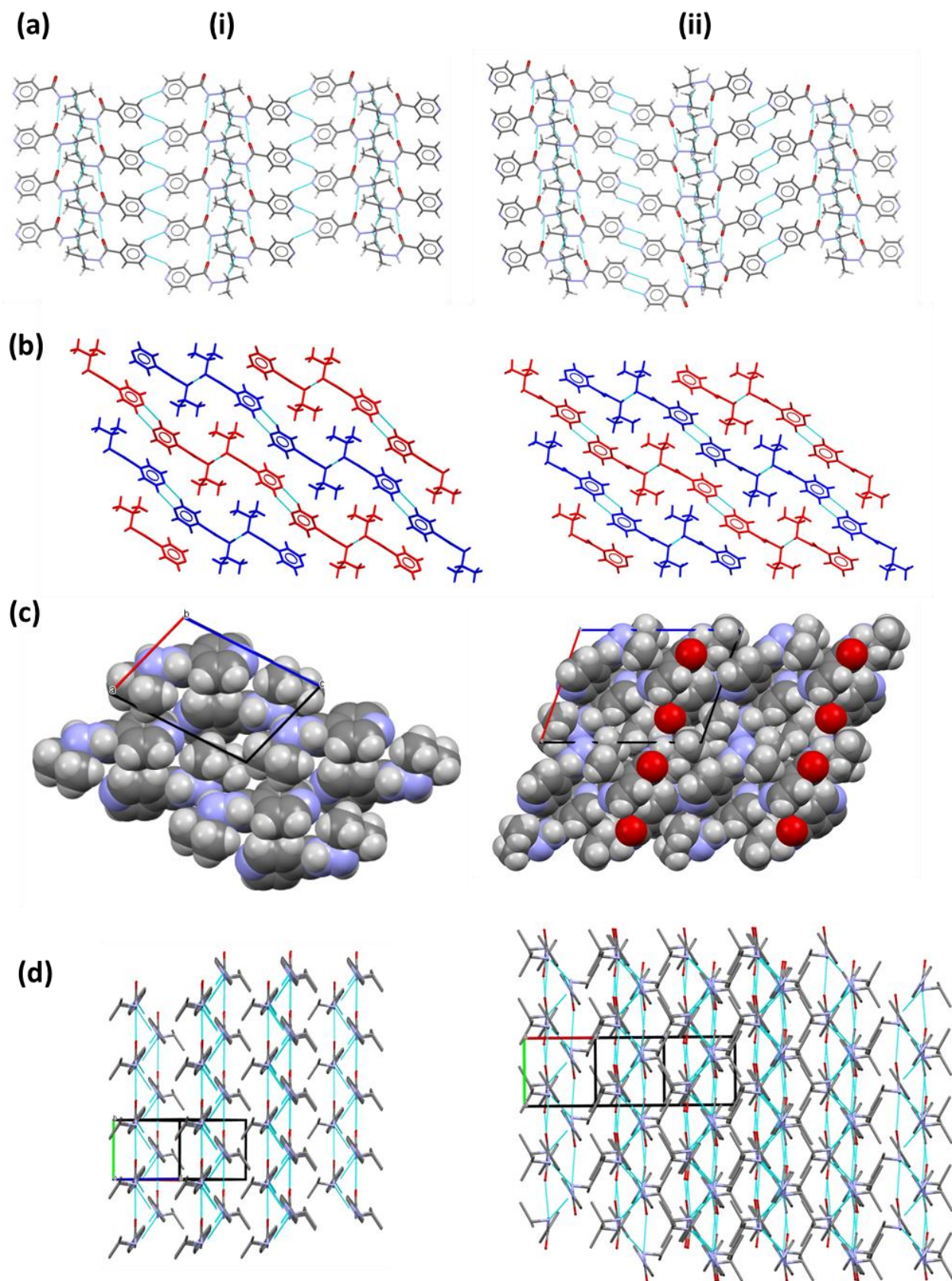


Figure S9 Comparison of packing for IPN (i) Form I and (ii) Form III. (a) IPN sheets comprised of H-bonding chains connected by pyridyl contacts and then joined forming by the H-bond between the amine groups of IPN molecules, (b) sheets visualised perpendicular H-bonding chains with alternative sheets coloured red and blue. Blue lines represent interactions between IPN molecules. (c) Spacefill representation of both forms viewing down the b-axis (d)Packing of the sheets demonstrating how the sheets pack. The anti-parallel H-bonding chains and different conformation in Form III all the methyl groups to pack more densely in between the sheets.

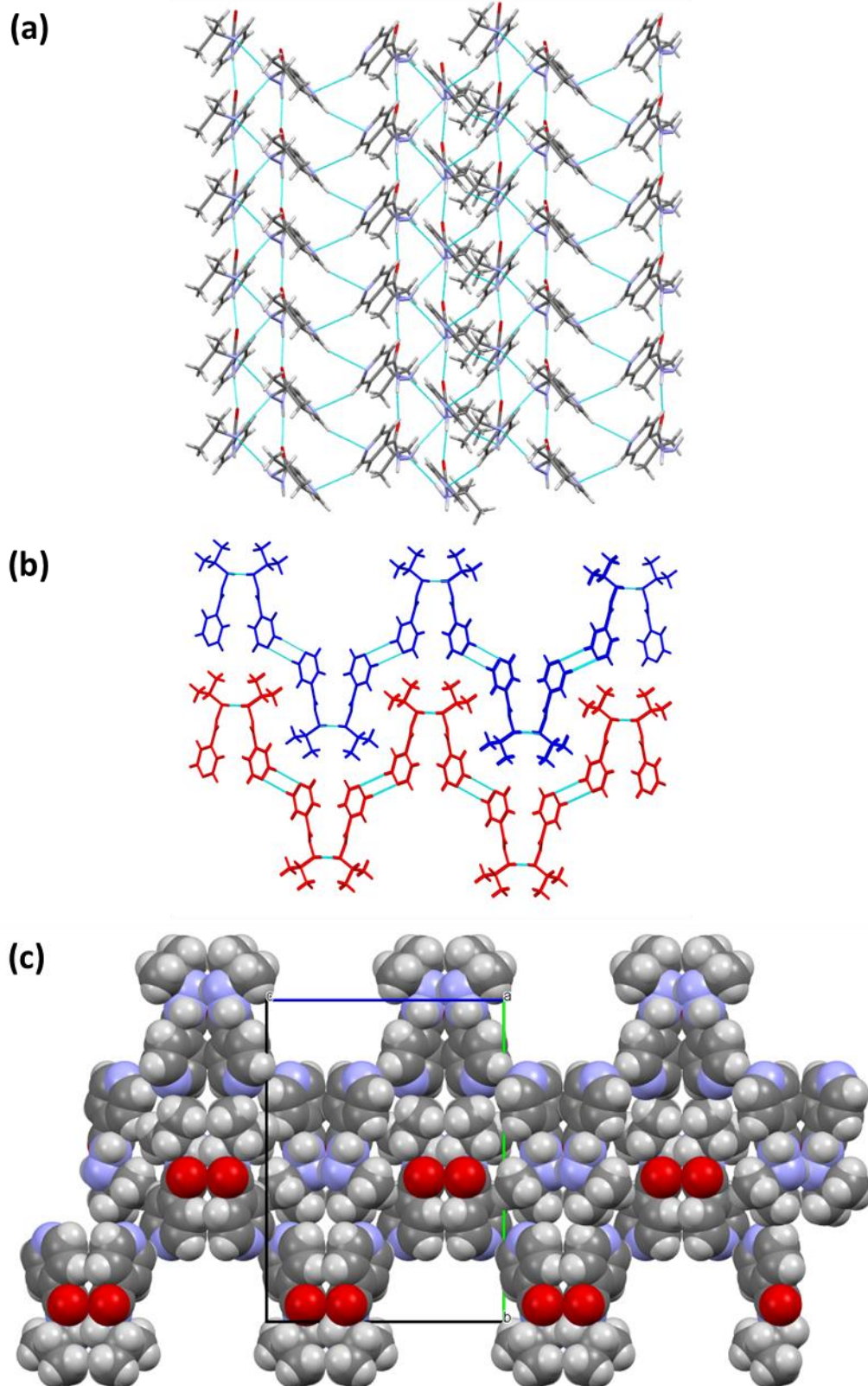


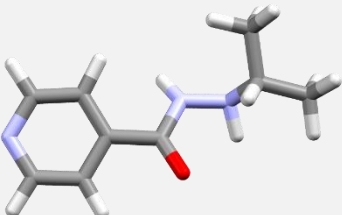
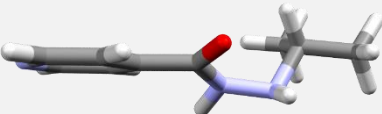
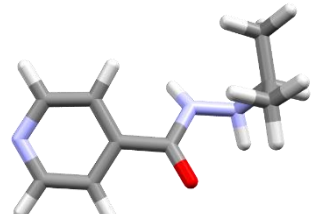
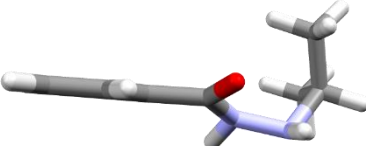
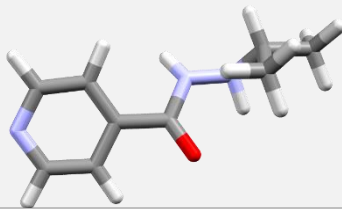
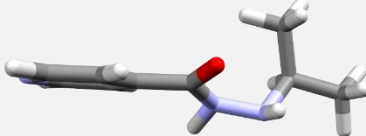
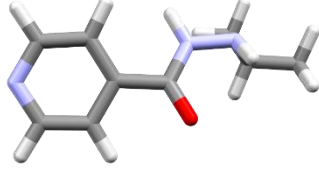
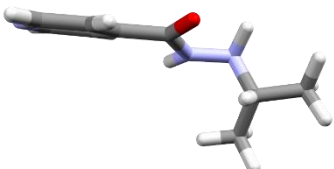
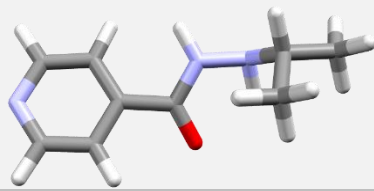
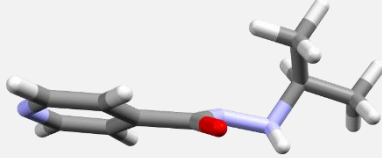
Figure S10 Packing for IPN Form II. (a) IPN sheets comprised of H-bonding chains connected by pyridyl contacts and then joined forming by the H-bond between the amine groups of IPN molecules, (b) sheets visualised perpendicular H-bonding chains with alternative sheets coloured red and blue. Blue lines represent interactions between IPN molecules. (c) Spacefill representation of both forms viewing down the a-axis

Computational Details

Molecular conformer generation

Initial molecular conformations for our CSP process were generated *via* the mixed low-mode/torsion conformer sampling procedure in Maestro²⁵, using the OPLS2005 force field.²⁶ It has been demonstrated that flexible drug-like molecules can adopt conformations in their crystal structures that are up to 20 kJ/mol higher in energy than the global minimum conformer in the gas phase.²⁷ Therefore, and to allow for errors in the force field, we selected all conformers within 25 kJ/mol of the minimum energy conformer for re-optimization and re-ranking using molecular DFT (B3LYP+GD3BJ/6-311G**) in Gaussian09.²⁸ Any duplicate conformers after re-optimization were removed.

The resulting 5 conformers for iproniazid are shown in the following table.

Conformer	Relative Energy / kJ/mol	Diagram	
A	0		
B	2.2		
C	2.3		
D	3.0		
E	5.4		

Space group selection for structure generation

Our choice of space groups to sample in our computational structure generation procedure was made based on the observed statistics of space group occurrence in the Cambridge Structural Database (CSD). Considering only $Z'=1$ structures of chiral molecules (both ISN and IPN are chiral), this yields the following 25 most common space groups, listed in order of decreasing frequency and representing 99% of $Z'=1$ structures in the CSD.

Space group number	International short symbol
14	$P 2_1 / c$
19	$P 2_1 2_1 2_1$
2	$P -1$
4	$P 2_1$
61	$P b c a$
15	$C 2 / c$
33	$P n a 2_1$
9	$C c$
29	$P c a 2_1$
5	$C 2$
1	$P 1$
60	$P b c n$
7	$P c$
18	$P 2_1 2_1 2$
43	$F d d 2$
56	$P c c n$
13	$P 2 / c$
88	$I 4_1 / a$
148	$R -3$
76	$P 4_1$
96	$P 4_3 2_1 2$
92	$P 4_1 2_1 2$
78	$P 4_3$
145	$P 3_2$
144	$P 3_1$

Multi-stage crystal structure minimization

Initially, our rigid-body minimization procedure occurs in a two-stage process – an initial minimization employing atom-centred point charges derived from the DFT molecular densities (fitted using GDMA^{29,30} and MULFIT^{31,32}, using the same DFT parameters as the conformer optimization) and an applied external pressure of 0.1 GPa, and a subsequent more accurate minimization with atom-centred distributed multipoles (obtained via GDMA) and no applied pressure. Non-electrostatic interactions are approximated using the FIT pairwise atomic repulsion-dispersion potential³³.

Within each space group, our stopping criterion for sampling was 10,000 successfully minimized (but not necessarily unique) crystal structures. Duplicate structures were removed by automated comparison of computed PXRD patterns obtained via the PLATON³⁴ program.

The plane-wave DFT optimizations were performed in the VASP^{35–38} software package, employing the PBE functional³⁹ and Grimme’s D3 dispersion correction⁴⁰ with Becke-Johnson damping (GD3BJ)⁴¹. Again, a two-stage optimization procedure was employed – initially only atomic positions were optimized with fixed cell parameters, then a second minimization allowed all degrees of freedom to relax. This procedure has been found to significantly improve rates of convergence by ourselves and others.^{42–44}

VASP optimizations were performed using a 500 eV energy cut-off for the plane-wave basis, with convergence tolerances of 1×10^{-7} eV per atom in the electronic minimization and 3×10^{-2} eV/Å in the forces in the geometry optimization, and Γ -centered k -point grids of 0.05 \AA^{-1} spacing. Final lattice energy rankings were obtained by performing a final single-point energy evaluation on the optimized structures using the same functional but with tighter convergence criteria and an increased 100 eV plane-wave energy cut-off. All calculations in VASP made use of the projector-augmented wave (PAW) method⁴⁵ and the standard supplied pseudopotentials.⁴⁶

Free energy calculations – effect of Debye model and of pressure

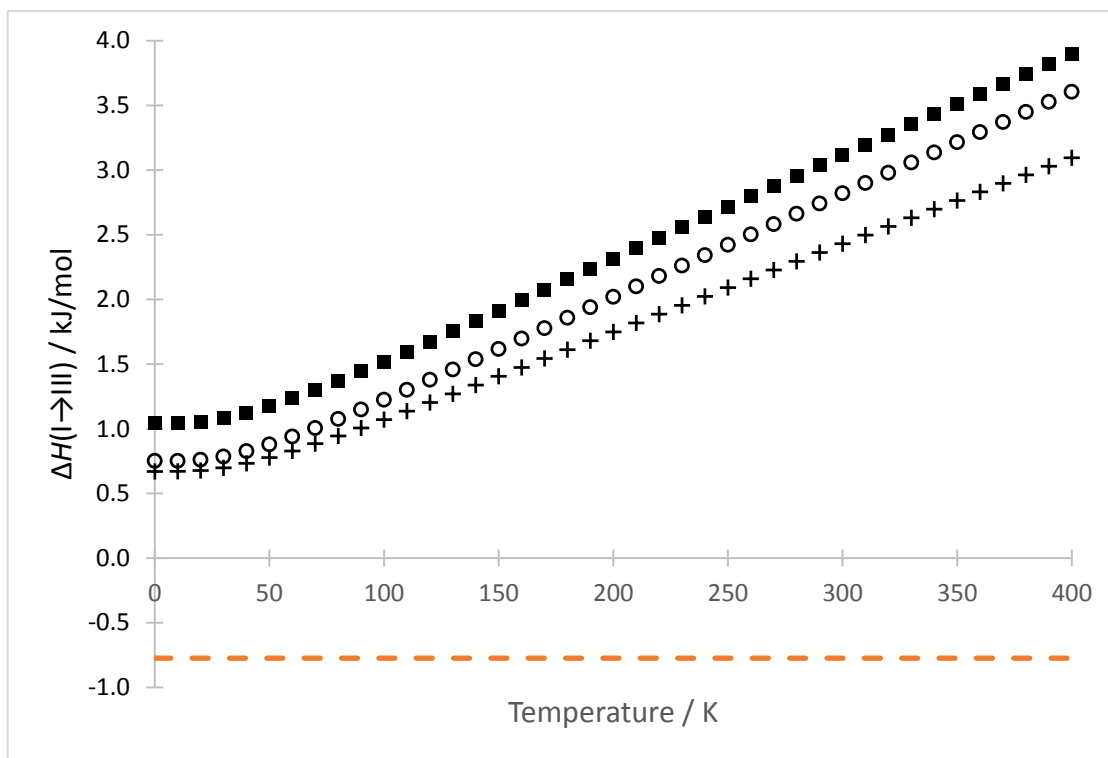


Figure S11: The computed free energy change on forming form III of iproniazid relative to Form I. Black squares are those obtained directly from integration over the density of states performed in Phonopy and determined by periodic DFT in VASP. Circles are the former values corrected with a Debye model for acoustic mode contributions, and crosses are values computed at a pressure of 2.4 GPa and with the Debye model correction. Note the free energy change is positive even at 0 K, indicating that the vibrational zero point energy alone is sufficient to re-rank Form III compared to the static lattice energy calculations (shown as the orange dashed line). Note also that the Debye model contribution to the difference is in this case largely independent of temperature.

Bibliography

- 1 S. R. Kennedy, C. D. Jones, D. S. Yufit, C. E. Nicholson, S. J. Cooper and J. W. Steed, *CrystEngComm*, 2018, **20**, 1390–1398.
- 2 A. Cayuela, S. R. Kennedy, M. L. Soriano, C. D. Jones, M. Valcárcel and J. W. Steed, *Chemical Science*, 2015, **6**, 6139–6146.
- 3 M. O. M. Piepenbrock, N. Clarke, J. A. Foster and J. W. Steed, *Chemical Communications*, 2011, **47**, 2095–2097.
- 4 O. V. Dolomanov, L. J. Bourhis, R. J. Gildea, J. a. K. Howard and H. Puschmann, *J Appl Cryst*, 2009, **42**, 339–341.
- 5 G. M. Sheldrick, *Acta Cryst A*, 2015, **71**, 3–8.
- 6 L. Merrill and W. A. Bassett, *Review of Scientific Instruments*, 1974, **45**, 290–294.
- 7 G. J. Piermarini, S. Block, J. D. Barnett and R. A. Forman, *Journal of Applied Physics*, 1975, **46**, 2774–2780.
- 8 S. A. Moggach, A. R. Lennie, C. A. Morrison, P. Richardson, F. A. Stefanowicz and J. E. Warren, *CrystEngComm*, 2010, **12**, 2587.
- 9 S. A. Moggach, D. R. Allan, S. Parsons and J. E. Warren, *Journal of Applied Crystallography*, 2008, **41**, 249–251.
- 10 A. Katrusiak, *Acta Crystallogr A Found Crystallogr*, 2008, **64**, 135–148.
- 11 M. A. Spackman and J. J. McKinnon, *CrystEngComm*, 2002, **4**, 378–392.
- 12 P. A. Wood, J. J. McKinnon, S. Parsons, E. Pidcock and M. A. Spackman, *CrystEngComm*, 2008, **10**, 368–376.
- 13 M. A. Spackman and D. Jayatilaka, *CrystEngComm*, 2009, **11**, 19–32.
- 14 F. P. A. Fabbiani, D. R. Allan, S. Parsons and C. R. Pulham, *CrystEngComm*, 2005, **7**, 179–186.
- 15 M. J. Turner, J. J. McKinnon, S. K. Wolff, D. J. Grimwood, D. Spackman, D. Jayatilaka and M. A. Spackman, *CrystalExplorer17*, University of Western Australia, 20117.
- 16 J. J. Novoa, M. Whangbo and J. M. Williams, *The Journal of Chemical Physics*, 1991, **94**, 4835–4841.
- 17 R. L. Rowley and T. Pakkanen, *The Journal of Chemical Physics*, 1999, **110**, 3368–3377.
- 18 E. G. Hohenstein and C. D. Sherrill, *J. Phys. Chem. A*, 2009, **113**, 878–886.
- 19 J. Zhang, Y. Gao, W. Yao, S. Li and F.-M. Tao, *Computational and Theoretical Chemistry*, 2014, **1049**, 82–89.
- 20 Q. A. Smith, M. S. Gordon and L. V. Slipchenko, *J. Phys. Chem. A*, 2011, **115**, 4598–4609.
- 21 C. F. Macrae, I. Sovago, S. J. Cottrell, P. T. A. Galek, P. McCabe, E. Pidcock, M. Platings, G. P. Shields, J. S. Stevens, M. Towler and P. A. Wood, *J Appl Cryst*, 2020, **53**, 226–235.
- 22 K. W. Galloway, S. A. Moggach, P. Parois, A. R. Lennie, J. E. Warren, E. K. Brechin, R. D. Peacock, R. Valiente, J. González, F. Rodríguez, S. Parsons and M. Murrie, *CrystEngComm*, 2010, **12**, 2516–2519.

- 23 S. Sobczak and A. Katrusiak, *Journal of Physical Chemistry C*, 2017, **121**, 2539–2545.
- 24 L. J. Barbour, *Chemical Communications*, 2006, 1163.
- 25 *Schrödinger: Maestro*, Schrödinger, LLC, 2019.
- 26 J. L. Banks, H. S. Beard, Y. Cao, A. E. Cho, W. Damm, R. Farid, A. K. Felts, T. A. Halgren, D. T. Mainz, J. R. Maple, R. Murphy, D. M. Philipp, M. P. Repasky, L. Y. Zhang, B. J. Berne, R. A. Friesner, E. Gallicchio and R. M. Levy, *Journal of Computational Chemistry*, 2005, **26**, 1752–1780.
- 27 H. P. G. Thompson and G. M. Day, *Chem. Sci.*, 2014, **5**, 3173–3182.
- 28 M. J. Frisch, G. W. Trucks, H. B. Schlegel, G. E. Scuseria, M. A. Robb, J. R. Cheeseman, G. Scalmani, V. Barone, B. Mennucci, G. A. Petersson, H. Nakatsuji, M. Caricato, X. Li, H. P. Hratchian, A. F. Izmaylov, J. Bloino, G. Zheng, J. L. Sonnenberg, M. Hada, M. Ehara, K. Toyota, R. Fukuda, J. Hasegawa, M. Ishida, T. Nakajima, Y. Honda, O. Kitao, H. Nakai, T. Vreven, J. A. Montgomery Jr., J. E. Peralta, F. Ogliaro, M. Bearpark, J. J. Heyd, E. Brothers, K. N. Kudin, V. N. Staroverov, R. Kobayashi, J. Normand, K. Raghavachari, A. Rendell, J. C. Burant, S. S. Iyengar, J. Tomasi, M. Cossi, N. Rega, J. M. Millam, M. Klene, J. E. Knox, J. B. Cross, V. Bakken, C. Adamo, J. Jaramillo, R. Gomperts, R. E. Stratmann, O. Yazyev, A. J. Austin, R. Cammi, C. Pomelli, J. W. Ochterski, R. L. Martin, K. Morokuma, V. G. Zakrzewski, G. A. Voth, P. Salvador, J. J. Dannenberg, S. Dapprich, A. D. Daniels, Ö. Farkas, J. B. Foresman, J. V. Ortiz, J. Cioslowski and D. J. Fox, *Gaussian09 Revision D.01*, .
- 29 A. J. Stone, *J. Chem. Theory Comput.*, 2005, **1**, 1128–1132.
- 30 A. J. STONE and M. ALDERTON, *Molecular Physics*, 2002, **100**, 221–233.
- 31 P. J. Winn, G. G. Ferenczy and C. A. Reynolds, *J. Phys. Chem. A*, 1997, **101**, 5437–5445.
- 32 G. G. Ferenczy, P. J. Winn and C. A. Reynolds, *J. Phys. Chem. A*, 1997, **101**, 5446–5455.
- 33 D. S. Coombes, S. L. Price, D. J. Willock and M. Leslie, *J. Phys. Chem.*, 1996, **100**, 7352–7360.
- 34 A. L. Spek, *Acta Cryst. Sect. D*, 2009, **65**, 148–155.
- 35 G. Kresse and J. Hafner, *Phys. Rev. B*, 1993, **47**, 558–561.
- 36 G. Kresse and J. Hafner, *Phys. Rev. B*, 1994, **49**, 14251–14269.
- 37 G. Kresse and J. Furthmüller, *Computational Materials Science*, 1996, **6**, 15–50.
- 38 G. Kresse and J. Furthmüller, *Phys. Rev. B*, 1996, **54**, 11169–11186.
- 39 J. P. Perdew, K. Burke and M. Ernzerhof, *Phys. Rev. Lett.*, 1996, **77**, 3865–3868.
- 40 S. Grimme, J. Antony, S. Ehrlich and H. Krieg, *J. Chem. Phys.*, , DOI:10.1063/1.3382344.
- 41 S. Grimme, S. Ehrlich and L. Goerigk, *J. Comp. Chem.*, 2011, **32**, 1456–1465.
- 42 C. R. Taylor and G. M. Day, *Crystal Growth & Design*, 2018, **18**, 892–904.
- 43 J. Moellmann and S. Grimme, *J. Phys. Chem. C*, 2014, **118**, 7615–7621.
- 44 M. A. Neumann and M.-A. Perrin, *J. Phys. Chem. B*, 2005, **109**, 15531–15541.
- 45 P. E. Blöchl, *Phys. Rev. B*, 1994, **50**, 17953–17979.
- 46 G. Kresse and D. Joubert, *Phys. Rev. B*, 1999, **59**, 1758–1775.
-